



Construction of ultrathin $\text{C}_3\text{N}_4/\text{Bi}_4\text{O}_5\text{I}_2$ layered nanojunctions via ionic liquid with enhanced photocatalytic performance and mechanism insight

Jiexiang Xia^{*}, Mengxia Ji, Jun Di, Bin Wang, Sheng Yin, Qi Zhang, Minqiang He, Huaming Li^{*}

School of Chemistry and Chemical Engineering, Institute for Energy Research, Jiangsu University, 301 Xuefu Road, Zhenjiang 212013, PR China

ARTICLE INFO

Article history:

Received 15 October 2015

Received in revised form 22 January 2016

Accepted 25 February 2016

Available online 27 February 2016

Keywords:

$\text{Bi}_4\text{O}_5\text{I}_2$

Ultrathin C_3N_4

Ionic liquid

Layered nanojunctions

Photocatalytic

ABSTRACT

A novel visible-light-driven ultrathin $\text{C}_3\text{N}_4/\text{Bi}_4\text{O}_5\text{I}_2$ layered nanojunctions photocatalyst was prepared via a facile solvothermal method in the presence of reactable ionic liquid 1-hexyl-3-methylimidazolium iodide ([Hmim]I). 1-hexyl-3-methylimidazolium iodide was served as I source, template and dispersing agent at the same time, which favored the formation of $\text{Bi}_4\text{O}_5\text{I}_2$ ultrasmall nanostructure and good dispersivity among the ultrathin C_3N_4 . A series of characterizations were employed to probe the structure, morphology, optical and electronic characteristics of the obtained ultrathin $\text{C}_3\text{N}_4/\text{Bi}_4\text{O}_5\text{I}_2$ layered nanojunctions. Experiment results show that the ultrasmall $\text{Bi}_4\text{O}_5\text{I}_2$ nanosheets were dispersed on the surface of ultrathin C_3N_4 uniformly and the compact heterostructures were constructed. The photocatalytic performance of the as-prepared samples was evaluated by the degradation of rhodamine B (RhB) and colorless endocrine disrupting chemical bisphenol A (BPA) under visible light irradiation. The ultrathin $\text{C}_3\text{N}_4/\text{Bi}_4\text{O}_5\text{I}_2$ layered nanojunctions displayed much higher photocatalytic activity than the pure $\text{Bi}_4\text{O}_5\text{I}_2$, in addition, 3 wt% ultrathin $\text{C}_3\text{N}_4/\text{Bi}_4\text{O}_5\text{I}_2$ exhibited the highest activity. The enhancement of photocatalytic activity was ascribed to the well-distribution for ultrasmall $\text{Bi}_4\text{O}_5\text{I}_2$ nanosheets on the ultrathin C_3N_4 surface and the formation of closely heterostructures that could favor the transfer and separation of photogenerated charge carriers. A possible photocatalytic mechanism based on the matched energy band structure and action mechanism of active species was proposed.

© 2016 Elsevier B.V. All rights reserved.

1. Introduction

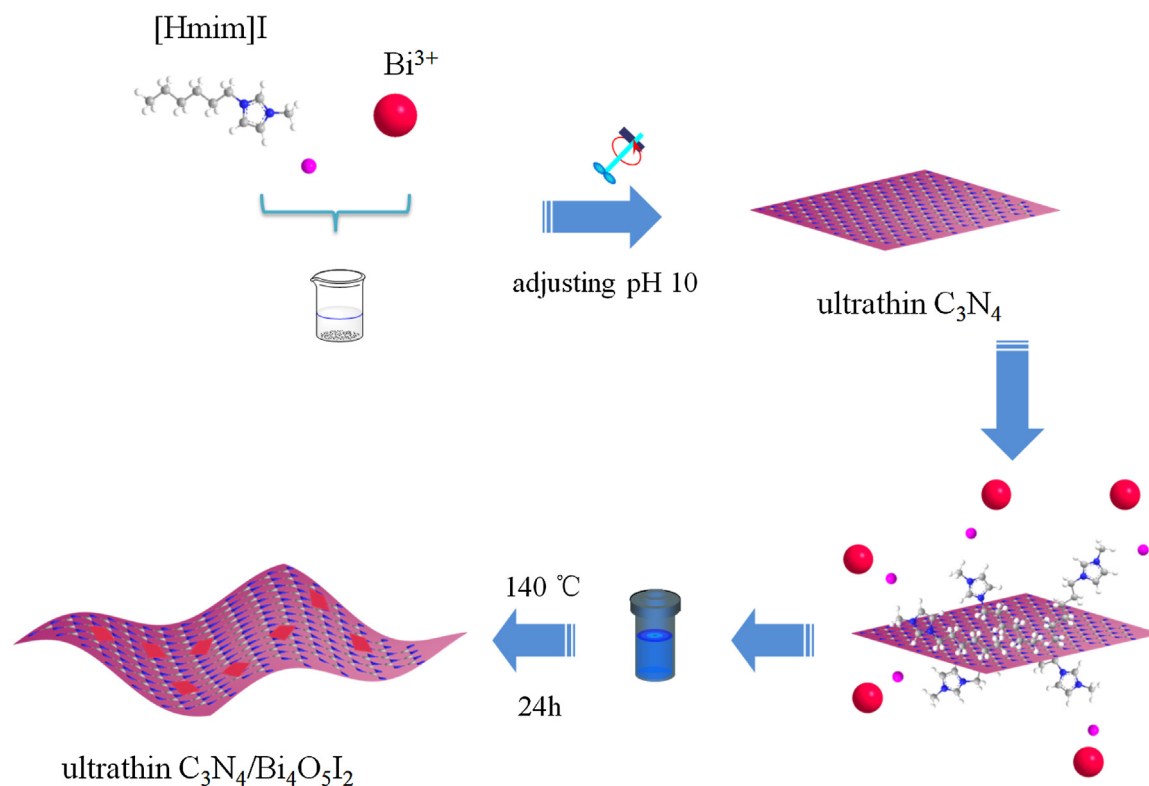
Environmental pollution and energy shortage are the most prominent and urgent problem in modern society, the emergence of semiconductor photocatalysts has aroused extensive interest among scientists [1–4]. Thereinto, bismuth-based compounds gradually appear in people's sight owing to their facile synthesis, high performance and environment friendly [5,6]. Among these compounds, bismuth oxyhalides as a new family of promising photocatalysts have been widely studied and reported [7,8].

Bismuth oxyhalides (BiOX ($\text{X} = \text{Cl}, \text{Br}, \text{I}$)), originally belong to the Sillén family, have demonstrated excellent photocatalytic activity arisen from their unique layered structure, $[\text{Bi}_2\text{O}_2]$ layer interleaved with double halogen atoms slabs [9–16]. BiOX ($\text{X} = \text{Cl}, \text{Br}, \text{I}$) exhibits remarkable photocatalytic performance for the rapid sep-

aration of photogenerated charge carriers, which resulted from the strong internal electric fields perpendicular to each layer [17,18]. However, for some limited defects, such as the low light absorption efficiency, the slow charge transfer and the high recombination rate of photogenerated electron-hole pairs, the photocatalytic activity of BiOX need to be further improved to meet the potential industrial applications. A series of strategies have been explored to increase the photocatalytic activity of bismuth oxyhalides, such as the exposed different crystal facets [19,20], surface modification [21,22], ion doping [23,24] and semiconductor compound etc [25–30]. Recently, the bismuth-rich strategy has been reported to be the effective strategies for improving the photocatalytic performance of bismuth oxyhalides, for instance, $\text{Bi}_{24}\text{O}_{31}\text{Br}_{10}$ [31], $\text{Bi}_4\text{O}_5\text{Br}_2$ [32] and $\text{Bi}_5\text{O}_7\text{I}$ [33]. Among these bismuth-rich oxyhalides, $\text{Bi}_4\text{O}_5\text{I}_2$ [34–39] shows the fascinating ability in removing the organic pollutant due to the suitable valence band (VB) and conduction band (CB) position. Based on the studies in photocatalysis field, it can be found that the construction of small size nanomaterials favor the improvement of photocatalytic activity. Up to now,

^{*} Corresponding authors.

E-mail addresses: xjx@ujs.edu.cn (J. Xia), lhm@ujs.edu.cn (H. Li).



Scheme 1. Schematic illustration of the formation process for ultrathin $C_3N_4/Bi_4O_5I_2$ material.

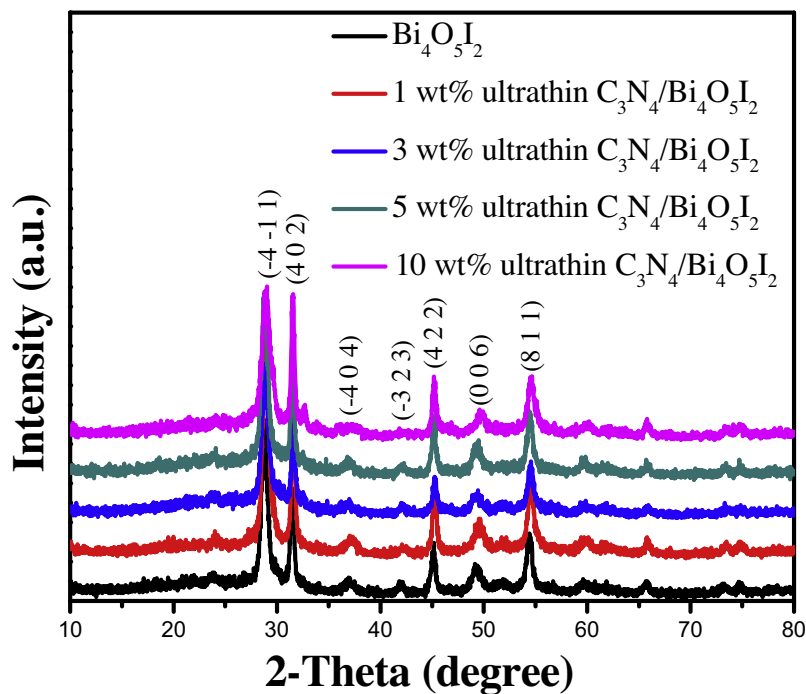


Fig 1. XRD patterns of the as-prepared pure $Bi_4O_5I_2$ and ultrathin $C_3N_4/Bi_4O_5I_2$ with different ultrathin C_3N_4 loading amount.

the $Bi_4O_5I_2$ was always assembled to 3D hierarchical micro/nano structure with diameter about several micrometers and the thickness of $Bi_4O_5I_2$ was limited to more than 15 nm. It was desirable to build the freestanding $Bi_4O_5I_2$ nanomaterials with ultrathin and ultrasmall structure so as to achieve superior photocatalytic activity.

Graphite-like carbon nitride (g- C_3N_4), the layered structure similar to graphene, is a polymeric organic nonmetallic material and the most stable phase of all allotropes under natural conditions [40]. The g- C_3N_4 is in the form of two-dimensional planes composed of tri-s-triazine composites and with weak van der Waals force among C-N layers, resulting in its high thermal and chemical stability. The

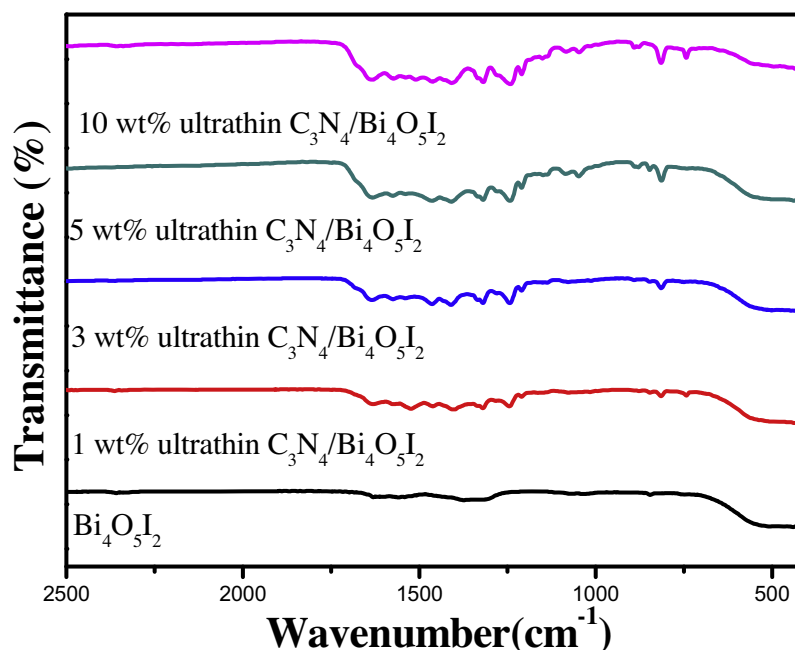


Fig. 2. FT-IR spectra of pure $\text{Bi}_4\text{O}_5\text{I}_2$ and ultrathin $\text{C}_3\text{N}_4/\text{Bi}_4\text{O}_5\text{I}_2$ with different contents of ultrathin C_3N_4 .

bandgap of g- C_3N_4 was calculated to be about 2.7 eV, and the CB and VB positions were respectively at -1.13 eV and 1.57 eV (vs normal hydrogen electrode), which enable a wide range of solar response in pollutants degradation [41]. The g- C_3N_4 -based photocatalysts have been utilized in the field of visible-light photocatalytic water splitting [42], CO_2 reduction [43], and organic syntheses [44]. However, the photocatalytic activity on the g- C_3N_4 is poor for the low quantum efficiency and high recombination rate of photo-generated electron-hole pairs [45]. Considering the materials with fewer layer structures could possess more exposed surfaces so as could supply more surface active sites, the efficient photocatalytic activity may be realized by constructing fewer layer ultrathin C_3N_4 [46]. At the same time, the ultrathin structure of fewer layer materials could enable the strikingly fast carrier transport from the inside to the surface, thus the higher separation efficiency of electron-hole pairs can be obtained [47].

Considering the superiority of $\text{Bi}_4\text{O}_5\text{I}_2$ and ultrathin C_3N_4 , if suitable approach was employed to construct tight junctions between $\text{Bi}_4\text{O}_5\text{I}_2$ and ultrathin C_3N_4 , the excellent photocatalytic activity may be obtained. At the same time, the C_3N_4 and $\text{Bi}_4\text{O}_5\text{I}_2$ have analogous layered structures, the lattice mismatch can be minimized, and heterojunctions with intimate contacts can be formed [48]. According to the previous research, they possess the advantages for controlling the formation of small-size nanoparticles and promoting the dispersion of nanomaterials [49]. Ionic liquids, as novel green solvents, play vital roles in the process of preparing inorganic nanomaterials for their excellent physical and chemical properties, such as thermo and chemical stability, dissolubility, lower toxicity and tractability. By the introduction of ionic liquid, it could act as reaction source, template agent, dispersing agent and capping agent simultaneously. Based on these advantages, the ionic liquid [Hmim]I was employed to improve the dispersibility of ultrathin C_3N_4 as well as controlling the formation of ultrasmall $\text{Bi}_4\text{O}_5\text{I}_2$ nanosheets so as nanojunctions can be constructed with maximum interfaces.

In this study, an attempt has been made to synthesize novel ultrathin $\text{C}_3\text{N}_4/\text{Bi}_4\text{O}_5\text{I}_2$ layered nanojunctions through a facile ionic liquid [Hmim]I (1-hexyl-3-methylimidazolium iodide) assisted solvothermal method. The introduction of reactable ionic liquid

[Hmim]I was acted as I source, capping agents for the formation of ultrasmall $\text{Bi}_4\text{O}_5\text{I}_2$ nanosheets, and used for improving the dispersity of ultrathin C_3N_4 , which was propitious to the combination of ultrathin C_3N_4 and $\text{Bi}_4\text{O}_5\text{I}_2$ together efficiently in the solution and further favor the construction of tight junction between the two. The photocatalytic activity of ultrathin $\text{C}_3\text{N}_4/\text{Bi}_4\text{O}_5\text{I}_2$ layered nanojunctions was evaluated by the degradation of rhodamine B (RhB) and colorless endocrine disrupting chemical bisphenol A (BPA) under visible light irradiation. Further more, the structure property of ultrathin $\text{C}_3\text{N}_4/\text{Bi}_4\text{O}_5\text{I}_2$ materials was discussed and a possible mechanism for the enhancement of photocatalytic performance was also proposed.

2. Experimental

2.1. Preparation of materials

Materials required for experiments were analytical reagent and used as yet unprocessed. The ionic liquid [Hmim]I (1-hexyl-3-methylimidazolium iodide) (99%) was purchased from Shanghai Chengjie Chemical Co. Ltd.

2.2. Synthesis of ultrathin $\text{C}_3\text{N}_4/\text{Bi}_4\text{O}_5\text{I}_2$ composite materials

The ultrathin C_3N_4 was synthesized according to our previous report and followed by calcination [27,46]. Typically synthesis process of ultrathin $\text{C}_3\text{N}_4/\text{Bi}_4\text{O}_5\text{I}_2$ composite materials as shown below: firstly, 1 mmol $\text{Bi}(\text{NO}_3)_3 \cdot 5\text{H}_2\text{O}$ was dissolved in 10 mL mannitol, then a certain amount of ultrathin C_3N_4 was added to form uniform suspension with continuous stirring at room temperature. After that, 10 mL mannitol solution dissolved 1 mmol [Hmim]I was added into the former suspension by drops with magnetic stirring. After dropping, the pH of the suspension was adjusted to 10 using 1 mol/L NaOH on top of stirring for 30 min. Then the mixture was poured into a 25 mL teflon-lined stainless-steel autoclave and heated at 140°C for 24 h in a drying oven. Subsequently the autoclave cooled to room temperature and the subsidence was washed several times with distilled water and absolute alcohol by centrifugation, and then dried at 60°C for hours (Scheme 1).

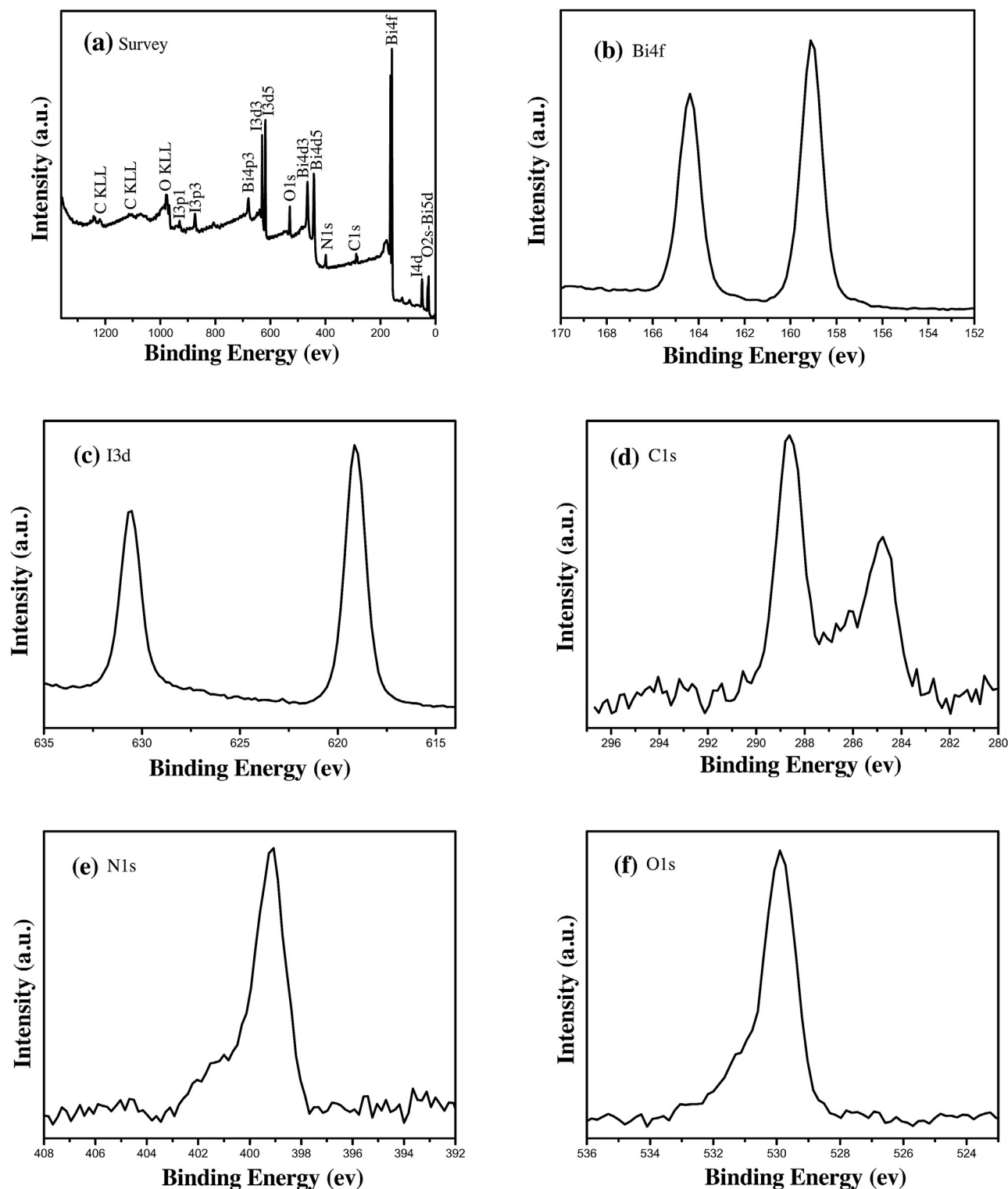


Fig. 3. XPS spectra 3 wt% ultrathin $C_3N_4/Bi_4O_5I_2$. (a) Survey of the sample; (b) Bi 4f; (c) I 3d; (d) C 1s; (e) N 1s; (f) O 1s.

2.3. Characterization

The crystalline phases of ultrathin $C_3N_4/Bi_4O_5I_2$ composite materials were determined by power X-ray diffraction (XRD) using a Shimadzu XRD-6000 X-ray diffractometer with $Cu-K\alpha$ radiation ($\lambda = 1.54 \text{ \AA}$). Transmission electron microscopy (TEM) micrographs were observed on a JEOL-JEM-2010 (JEOL, Japan) operated at 200 kV. UV–vis diffuse reflection spectra (DRS) was recorded on

an UV–vis spectrophotometer (UV-2450 Shimadzu Corporation, Japan) in the range of 200–800 nm ($BaSO_4$ powder used as the substrate). Fourier transform infrared (FT-IR) spectra were measured on a Nicolet Model Nexus 470 FT-IR equipment using KBr pellet technic. X-ray photoelectron spectroscopy (XPS) analysis was taken on an ESCALab MKII X-ray photo-electron spectrometer using the $Mg-K\alpha$ radiation. The nitrogen adsorption-desorption isotherms

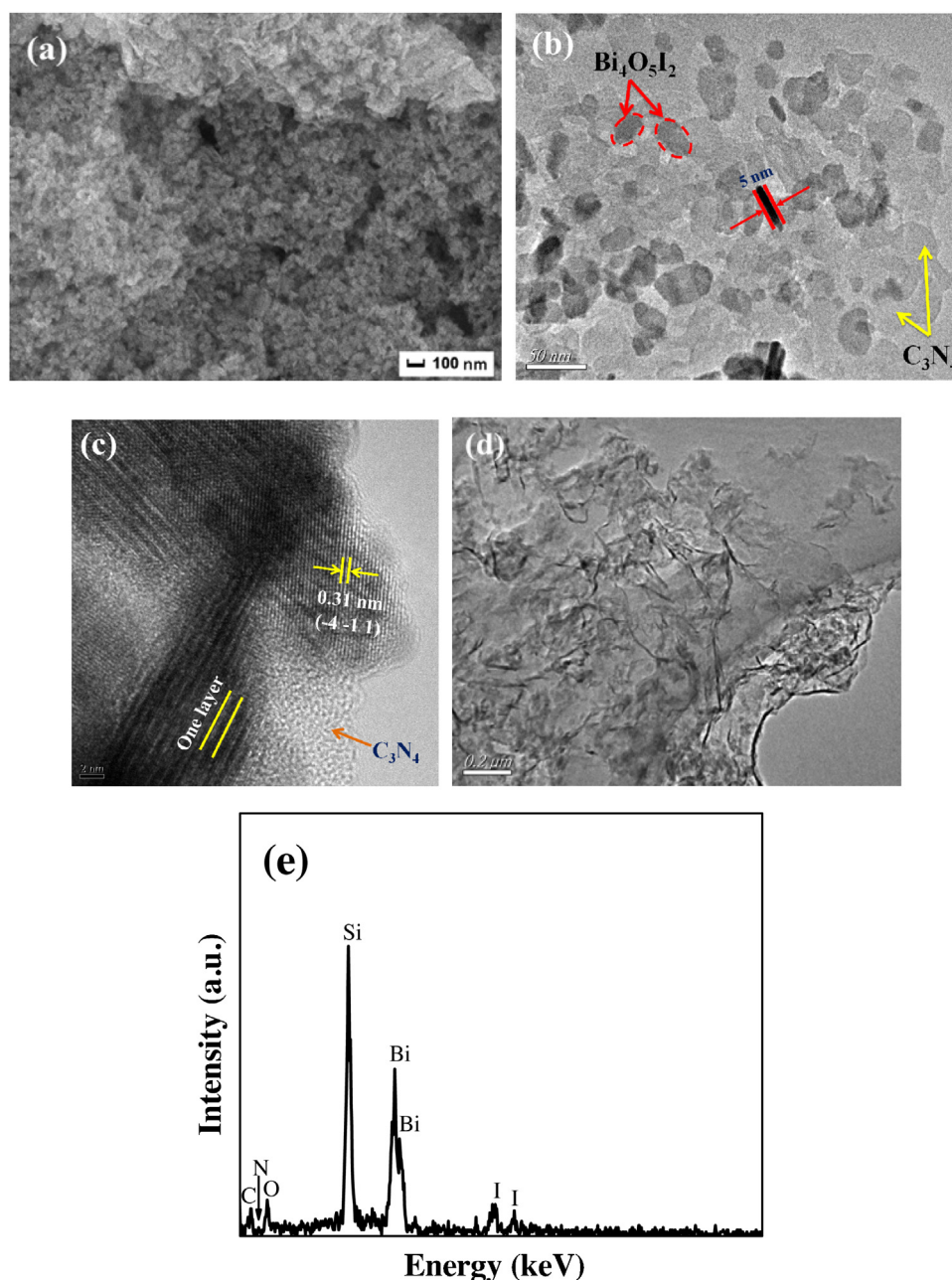


Fig. 4. SEM, TEM and HRTEM images of the 10 wt% ultrathin $C_3N_4/Bi_4O_5I_2$: (a) the SEM image; (b) the high magnification TEM image; (c) the high-resolution TEM image. (d) the TEM image of ultrathin C_3N_4 . (e) EDS of the 10 wt% ultrathin $C_3N_4/Bi_4O_5I_2$.

at 77 K were researched using a TriStar II 3020 surface area and porosity analyzer (Micromeritics Instrument Corporation, USA).

2.4. Photocatalytic activity

Photocatalytic degradation experiments of $Bi_4O_5I_2$ and ultrathin $C_3N_4/Bi_4O_5I_2$ composite materials were performed in a Pyrex photocatalytic reactor equipped with a 300 W Xe lamp and a 400 nm cutoff filter as the lamp-house. All photocatalytic reactions were implemented under the same conditions: a reactor with 20 mg as-synthesized samples for RhB aqueous solution or 50 mg samples for BPA aqueous solution scattered in 10 mg L^{-1} 100 mL organic pollutant were placed in a container with continuous stirring. To achieve the adsorption-desorption equilibrium, the mixed solution was stirred for 30 min in the darkness. During the photocatalytic degradation process, about 3 mL reaction solution measured out in

certain time was estimated on a UV-vis spectro-photometer (UV-2450, Shimadzu), at the same time the absorption wavelength of 553 nm. The residue amount of BPA was analyzed by high performance liquid chromatography (HPLC). The Agilent HPLC system was equipped with two Varian ProStar210 pumps, an Agilent T C-C (18) column, and a Varian ProStar325 UV-vis detector at 230 nm. The mobile phase was a mixed methanol aqueous solution and the volume ratio was 75: 25. The flow rate was 1.0 mL min^{-1} .

2.5. Photoelectrochemical properties

To investigate the transition of photo-induced carriers of prepared materials, ultrathin $C_3N_4/Bi_4O_5I_2$ composite materials electrodes were prepared to test the photocurrent performance using an electrochemical analyzer with a standard three-electrode system. A platinum wire was used as counter electrode and a

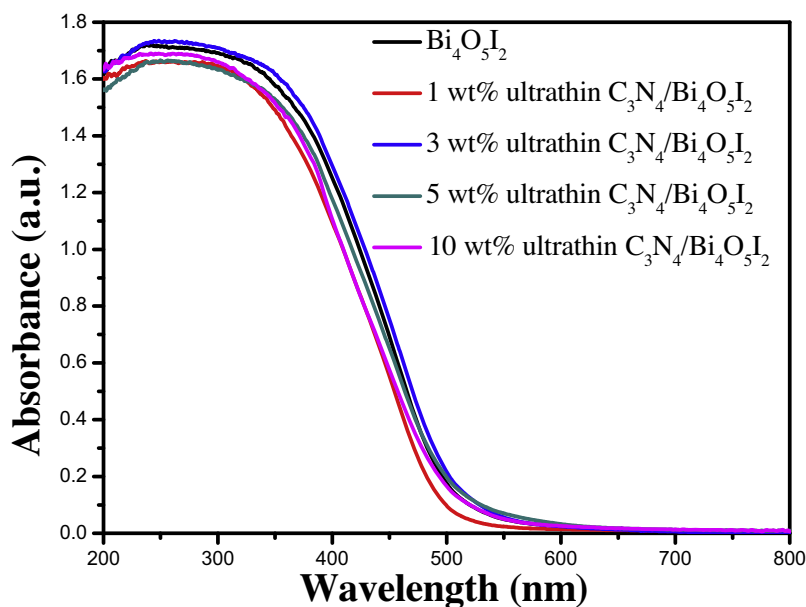


Fig. 5. The optical absorption spectroscopy of ultrathin $C_3N_4/Bi_4O_5I_2$ materials.

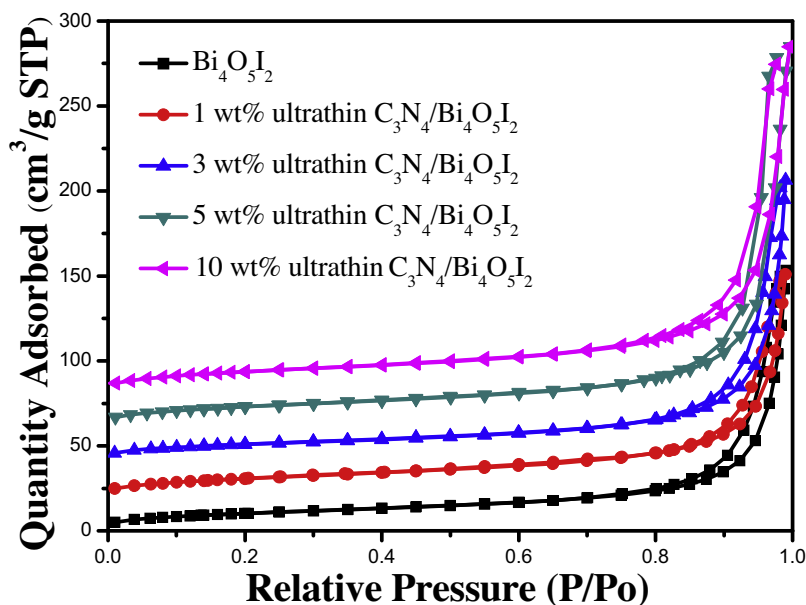


Fig. 6. Nitrogen adsorption-desorption isotherm of ultrathin $C_3N_4/Bi_4O_5I_2$ materials.

saturated Ag/AgCl electrode was employed as reference electrode, while the ITO glass ($0.5 \times 1 \text{ cm}^2$) covered with ultrathin $C_3N_4/Bi_4O_5I_2$ catalyst (0.1 mg) was served as working electrode, respectively. A 500 W xenon lamp equipped with a 400 nm cut-off filter was used as the photosource. The photocurrent and EIS were performed in a 0.1 M phosphate buffered saline aqueous solution (pH=7) and a 0.1 M KCl solution containing 5 mM $[Fe(CN)_6]^{3-}/[Fe(CN)_6]^{4-}$, respectively. Unless conditions were identical among all electrochemical measurements.

3. Results and Discussion

To identify the crystalline phase structure and purity of the prepared materials, the powder X-ray diffractometer was employed. By comparison, these diffraction peaks as shown in Fig. 1 located at 28.8° ($-4-11$), 31.5° (402), 36.9° (402), 42.1° (-323), 45.1°

(422), 49.3° (006) and 54.4° (811) were coincident with the previous reports [34]. However, no typical patterns of C_3N_4 were found in the ultrathin $C_3N_4/Bi_4O_5I_2$ composite materials as a result of the low ultrathin C_3N_4 content in the samples. Among the XRD analysis, no other impurity peaks were noticed, which confirmed the high purity of the ultrathin $C_3N_4/Bi_4O_5I_2$ materials.

To further confirm the existence of ultrathin C_3N_4 , Fourier transform infrared analysis was carried out. Fig. 2 exhibits the FT-IR spectra of pure $Bi_4O_5I_2$ and ultrathin $C_3N_4/Bi_4O_5I_2$ composite materials. Compared to the pure $Bi_4O_5I_2$, the strong bands in the $1200-1650 \text{ cm}^{-1}$ region for ultrathin $C_3N_4/Bi_4O_5I_2$ composites were found in the spectrum, with the peaks at 1243, 1322, 1411, 1576, and 1635 cm^{-1} , which corresponded to the typical stretching vibration modes of heptazine heterocyclic ring units [12]. In addition a representative peak appeared at 810 cm^{-1} was assigned to the characteristic breathing mode of s-triazine, which indicated

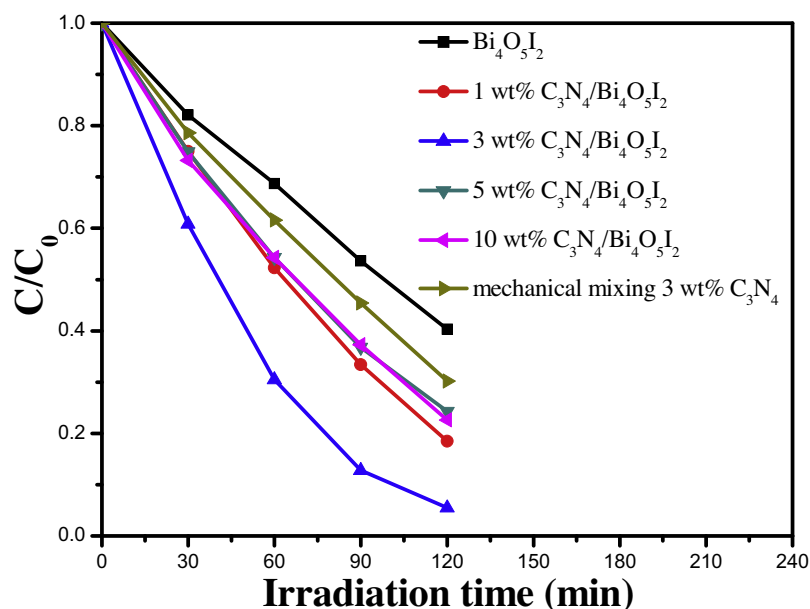


Fig. 7. Photocatalytic degradation of RhB in the presence of pure $\text{Bi}_4\text{O}_5\text{I}_2$, ultrathin $\text{C}_3\text{N}_4/\text{Bi}_4\text{O}_5\text{I}_2$ materials and the mechanical mixing 3 wt% ultrathin $\text{C}_3\text{N}_4/\text{Bi}_4\text{O}_5\text{I}_2$ material under visible light irradiation.

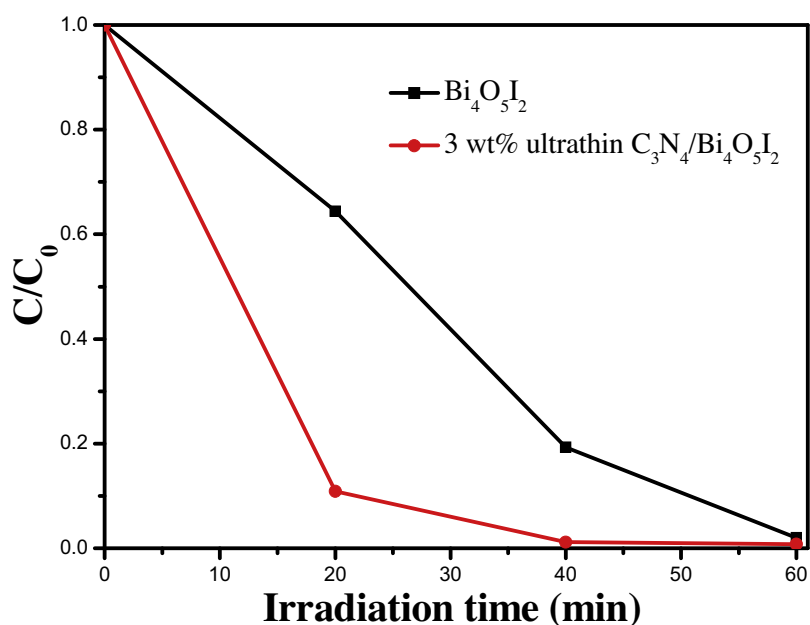


Fig. 8. Photocatalytic degradation of BPA in the presence of pure $\text{Bi}_4\text{O}_5\text{I}_2$ and 3 wt% ultrathin $\text{C}_3\text{N}_4/\text{Bi}_4\text{O}_5\text{I}_2$ under visible light irradiation.

that ultrathin C_3N_4 was successfully introduced in the composites. The FT-IR analysis shows that $\text{Bi}_4\text{O}_5\text{I}_2$ and ultrathin C_3N_4 have been combined together successfully.

XPS is commonly used to investigate the components and surface properties of the ultrathin $\text{C}_3\text{N}_4/\text{Bi}_4\text{O}_5\text{I}_2$ sample. XPS survey spectra and high-resolution XPS spectra of the Bi 4f, I 3d, C 1s, O 1s and N 1s for 10 wt% ultrathin $\text{C}_3\text{N}_4/\text{Bi}_4\text{O}_5\text{I}_2$ are displayed in Fig. 3. The survey XPS spectrum (Fig. 3a) shows that the main elements on the surface of the sample are Bi, I, O, C and N. The peaks at 159.1 eV and 164.3 eV in high-resolution Bi 4f spectra (Fig. 3b) were attributed to Bi 4f_{7/2} and Bi 4f_{5/2}, respectively. Fig. 3c shows high-resolution I 3d spectra of the composites, in which the two typical peaks located at 619.1 eV and 630.6 eV could be assigned to I 3d_{3/2} and I 3d_{5/2}, respectively. Two obvious peaks at binding

energies 284.4 eV and 288.6 eV of C 1s XPS spectra were shown in Fig. 3d. The peak at 284.4 eV could be ascribed to carbon (C–C, C=C) and the peak at 288.6 eV was assigned to defect-containing sp²-bonded carbon (N–C=N) [50,51]. The peak binding energies of 399.1 eV (Fig. 3e) and 529.9 eV (Fig. 3f) were attributed to N 1s and O 1s, respectively. All of these XPS results further confirmed the coexistence of ultrathin C_3N_4 and $\text{Bi}_4\text{O}_5\text{I}_2$, which is in accordance with the FT-IR analysis.

The surface morphology and microstructure of the 10 wt% ultrathin $\text{C}_3\text{N}_4/\text{Bi}_4\text{O}_5\text{I}_2$ layered nanojunctions were determined by field-emission SEM and TEM and the results are exhibited in Fig. 4. As shown in Fig. 4a, many uniform nanoparticles with the ultrasmall size can be seen from SEM image. In order to further determine the detailed structural information of the ultrathin

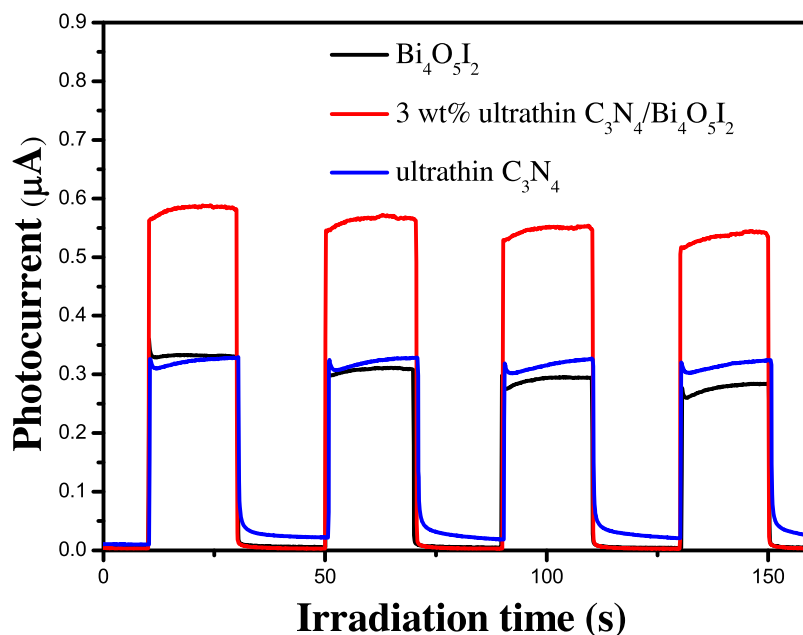


Fig. 9. Transient photocurrent responses for the pure $\text{Bi}_4\text{O}_5\text{I}_2$, 3 wt% ultrathin $\text{C}_3\text{N}_4/\text{Bi}_4\text{O}_5\text{I}_2$ and ultrathin C_3N_4 samples.

$\text{C}_3\text{N}_4/\text{Bi}_4\text{O}_5\text{I}_2$ material, TEM analysis was carried out and the results were shown in Fig. 4b. In Fig. 4b, a transparent structure that could be caught easily, which indicated the morphology of C_3N_4 in $\text{C}_3\text{N}_4/\text{Bi}_4\text{O}_5\text{I}_2$ composite was the ultrathin structure. It can be seen that the thickness of ultrasmall $\text{Bi}_4\text{O}_5\text{I}_2$ nanosheets was about 6 nm, and these nanosheets dispersed on the surface of ultrathin C_3N_4 uniformly. The corresponding high-resolution TEM (HRTEM) image of the ultrathin $\text{C}_3\text{N}_4/\text{Bi}_4\text{O}_5\text{I}_2$ was shown in Fig. 4c. It can be seen distinctly that the coexistence of ultrathin C_3N_4 and $\text{Bi}_4\text{O}_5\text{I}_2$ nanomaterials, and the uniform interplanar spacing of crystalline domain were determined to be ~ 0.31 nm, which was corresponding to the $(-4-11)$ plane of the monoclinic $\text{Bi}_4\text{O}_5\text{I}_2$. As shown in Fig. 4d, many folds can be seen on the surface of the ultrathin C_3N_4 . From the AFM analysis (Fig. S1), the majority of the sheets pos-

sessed an average height of about 0.9 nm, which was in accord with the TEM analysis. These results further indicated the as-prepared C_3N_4 materials possess ultrathin structure. From the energy dispersive X-ray spectroscopy (EDS) in Fig. 4e, the sample was consist of Bi, O, I, C, N and O elements, that further confirming the as-prepared material was $\text{C}_3\text{N}_4/\text{Bi}_4\text{O}_5\text{I}_2$ composite.

Fig. 5 reveals the optical properties of ultrathin $\text{C}_3\text{N}_4/\text{Bi}_4\text{O}_5\text{I}_2$ materials examined by UV-vis diffuse reflectance spectrum. The absorption region of as-prepared $\text{Bi}_4\text{O}_5\text{I}_2$ nanosheets was about 200–520 nm, which enabled $\text{Bi}_4\text{O}_5\text{I}_2$ nanomaterial to possess superior light absorption ability. After the introduction of ultrathin C_3N_4 , a certain blue shift phenomenon for ultrathin $\text{C}_3\text{N}_4/\text{Bi}_4\text{O}_5\text{I}_2$ composites could be observed distinctly, indicating the absorption of visible light by composites decreased.

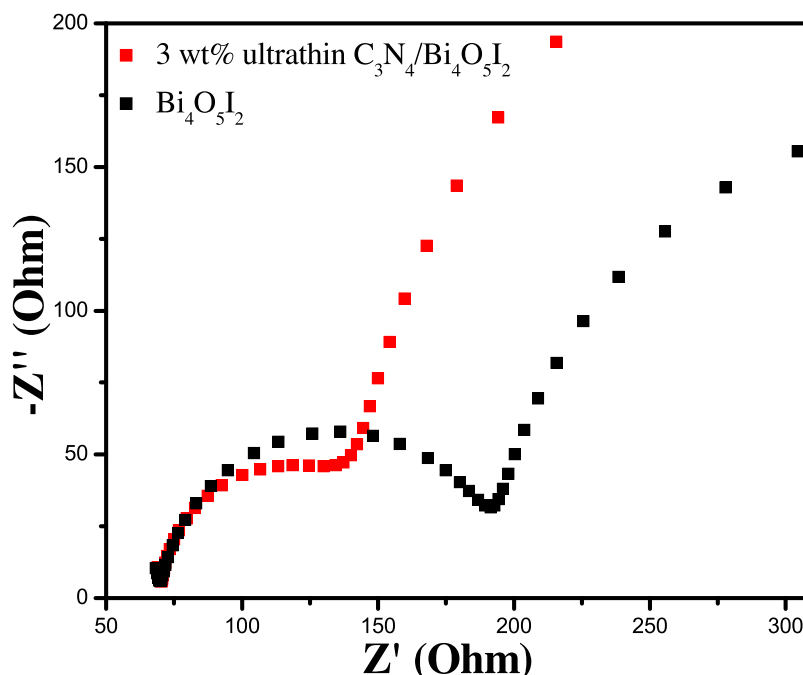


Fig. 10. Electrochemical impedance spectroscopy of pure $\text{Bi}_4\text{O}_5\text{I}_2$ and 3 wt% ultrathin $\text{C}_3\text{N}_4/\text{Bi}_4\text{O}_5\text{I}_2$ samples.

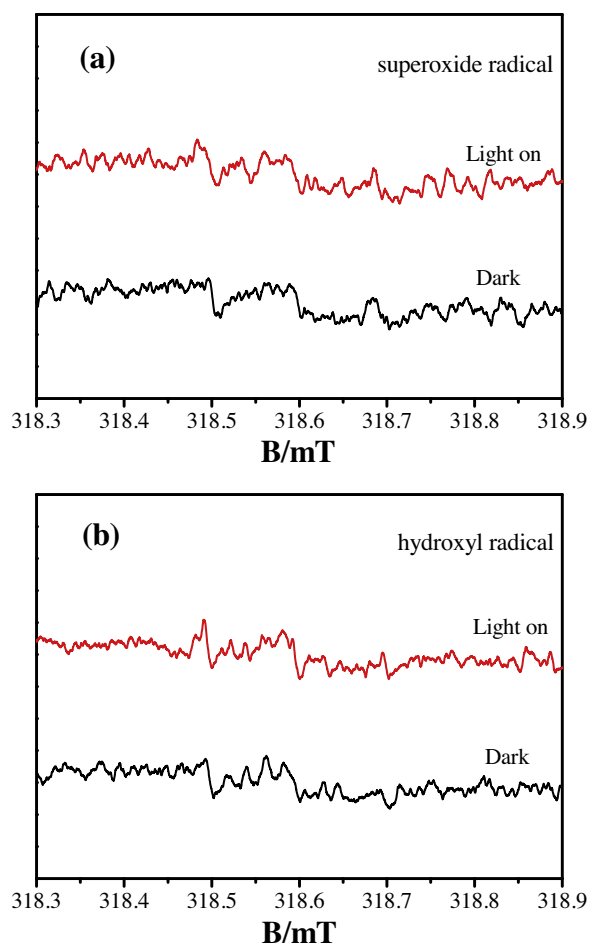


Fig. 11. ESR spectra of radical adducts trapped by DMPO in ultrathin $C_3N_4/Bi_4O_5I_2$ materials (a) methanol dispersion and (b) aqueous dispersion under visible light irradiation.

As shown in Fig. 6, the BET specific surface areas of the ultrathin $C_3N_4/Bi_4O_5I_2$ materials were investigated via nitrogen absorption–desorption isotherm. The BET specific surface area of $Bi_4O_5I_2$ samples was calculated to be $38.13 \text{ m}^2 \text{ g}^{-1}$. Moreover, the BET specific surface area increased gradually with the enhanced amount of ultrathin C_3N_4 , and calculated to be $40.87 \text{ m}^2 \text{ g}^{-1}$, $41.07 \text{ m}^2 \text{ g}^{-1}$, $47.22 \text{ m}^2 \text{ g}^{-1}$, $49.85 \text{ m}^2 \text{ g}^{-1}$ for 1 wt%, 3 wt%, 5 wt%, 10 wt% ultrathin $C_3N_4/Bi_4O_5I_2$ materials, respectively. Since the C_3N_4 materials with ultrathin structure had larger surface area, the introduction of ultrathin C_3N_4 could enlarge specific surface area of composite materials. Generally, the larger specific surface area can make catalysts adequately contact with pollutants and provide more reaction sites to produce more active species in the photodegradation process [52,53].

The photocatalytic activity of pure $Bi_4O_5I_2$, ultrathin $C_3N_4/Bi_4O_5I_2$ materials and the mechanical mixing 3 wt% ultrathin $C_3N_4/Bi_4O_5I_2$ material was evaluated by adopting RhB as the target pollutant under visible light irradiation. As shown in Fig. 7, it is easy to see that adding different amounts of ultrathin C_3N_4 could improve the photocatalytic activity of $Bi_4O_5I_2$, among these, 3 wt% ultrathin $C_3N_4/Bi_4O_5I_2$ exhibited the highest activity. For comparison, the photocatalytic activity of degradation RhB for the 3 wt% ultrathin C_3N_4 and $Bi_4O_5I_2$ materials mixed by physical means was carried out, and the results exhibited that 3 wt% ultrathin $C_3N_4/Bi_4O_5I_2$ exhibited higher activity than that $Bi_4O_5I_2$ materials mixed with 3 wt% ultrathin C_3N_4 , which implied the facile solvothermal method made the two materials can compound together adequately to receive larger surface area and provide more active sites. After irradiation for 60 min, only 31% of RhB was photodegraded by pure $Bi_4O_5I_2$, while the photolysis of RhB was up to 70% in the presence of 3 wt% ultrathin $C_3N_4/Bi_4O_5I_2$. When the content was higher than 3 wt%, there was a decreased rate in the photo-degradation of RhB. That could be attributed to the excessive ultrathin C_3N_4 coating on the surface of $Bi_4O_5I_2$, which inhibited the $Bi_4O_5I_2$ absorbing visible light and resulted in the depressed photocatalytic degradation efficiency. These results indicated that the absorption of visible light or the specific surface area was not the crucial role in this system for the enhanced activity.

BPA, as the important organic chemical raw materials and derivatives of phenol and acetone, has been widely used in human daily life. However, research shows that the residue of BPA in the

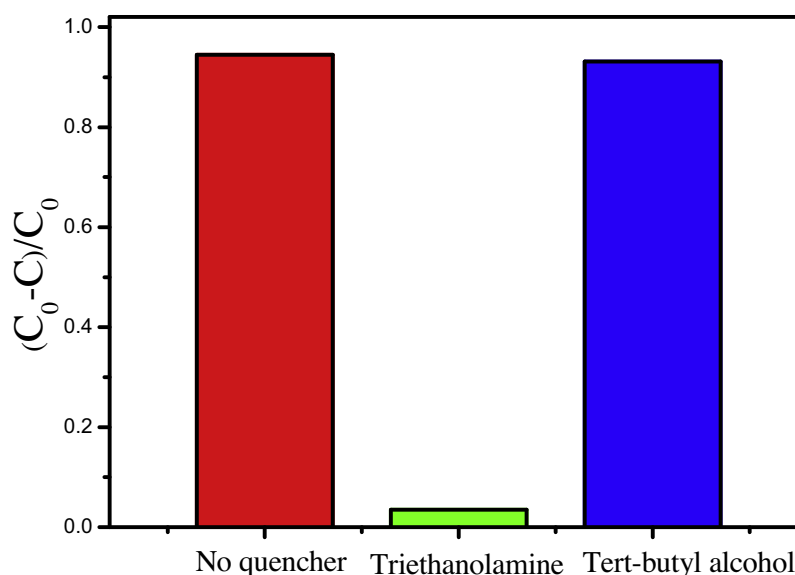


Fig. 12. Free radicals trapping experiment of 3 wt% ultrathin $C_3N_4/Bi_4O_5I_2$ material under visible light irradiation.

environment could cause endocrine disorders and threaten the health of the fetus and children. Therefore, efficient degradation of BPA has become extremely important. Fig. 8 shows the photocatalytic degradation experiment of BPA under the visible light by pure $\text{Bi}_4\text{O}_5\text{I}_2$ and ultrathin $\text{C}_3\text{N}_4/\text{Bi}_4\text{O}_5\text{I}_2$ materials. After 20 min, nearly 90% of BPA was removed over 3 wt% ultrathin $\text{C}_3\text{N}_4/\text{Bi}_4\text{O}_5\text{I}_2$ composites, which the degradation efficiency of $\text{Bi}_4\text{O}_5\text{I}_2$ was only about 35% under the same condition. Therefore, the 3 wt% ultrathin $\text{C}_3\text{N}_4/\text{Bi}_4\text{O}_5\text{I}_2$ photocatalyst exhibited the better photocatalytic activity. It can be seen that the introduction of ultrathin C_3N_4 could favor the enhancement of photocatalytic performance. The dramatic activity of ultrathin $\text{C}_3\text{N}_4/\text{Bi}_4\text{O}_5\text{I}_2$ materials may let ultrathin $\text{C}_3\text{N}_4/\text{Bi}_4\text{O}_5\text{I}_2$ become valuable photocatalytic material in potential applications for environmental protection.

The degradation intermediates during the photocatalytic process of degrading BPA over 3 wt% ultrathin $\text{C}_3\text{N}_4/\text{Bi}_4\text{O}_5\text{I}_2$ material were investigated by LC–MS analysis, as shown in Fig. S2a. It can be observed directly that BPA at m/z 227.48 eluted at a retention time of 5.61 min (Fig. S2b). Only one intermediate at m/z 198.21 was detected by LC–MS analysis (Fig. S2c). The concentration of that intermediate increased to its maximum concentration after irradiation for 20 min, then decreased gradually for the later 40 min, these results demonstrated that the intermediate engendered in the photocatalytic degradation was degraded in succession after a period of photodegradation time. Meanwhile, the degradation procedure for BPA by 3 wt% ultrathin $\text{C}_3\text{N}_4/\text{Bi}_4\text{O}_5\text{I}_2$ material was proposed as Fig. S3.

The transient photocurrent responses analysis was employed to investigate the separation of electrons and holes of the as-prepared materials (Fig. 9). In general, a higher photocurrent implies the produce of more electrons under illumination and could further promote the photocatalytic activity. Apparently, 3 wt% ultrathin $\text{C}_3\text{N}_4/\text{Bi}_4\text{O}_5\text{I}_2$ exhibited higher photocurrent intensity than the pure $\text{Bi}_4\text{O}_5\text{I}_2$ and ultrathin C_3N_4 materials, at the same time, both of them remained relatively stable, which testified that the formation of close heterojunction among ultrathin $\text{C}_3\text{N}_4/\text{Bi}_4\text{O}_5\text{I}_2$ layered nanojunctions advanced the separation of photo-induced charge carriers and thus enabled the higher photocatalytic activity [54].

Fig. 10 reveals the electrochemical impedance spectroscopy (EIS) of pure $\text{Bi}_4\text{O}_5\text{I}_2$ and 3 wt% ultrathin $\text{C}_3\text{N}_4/\text{Bi}_4\text{O}_5\text{I}_2$ samples. The analysis clearly showed that the diameter of Nyquist circle in the high frequency region of the 3 wt% ultrathin $\text{C}_3\text{N}_4/\text{Bi}_4\text{O}_5\text{I}_2$ electrode was smaller than that of pure $\text{Bi}_4\text{O}_5\text{I}_2$, which indicated that ultrathin structure C_3N_4 compounded with $\text{Bi}_4\text{O}_5\text{I}_2$ successfully and formed a compact interface contact. Conjugated π -bond in ultrathin C_3N_4 is beneficial to the transfer of electrons so that ultrathin $\text{C}_3\text{N}_4/\text{Bi}_4\text{O}_5\text{I}_2$ composite possessed the smaller resistance [55]. The satisfactory in-contact of ultrathin $\text{C}_3\text{N}_4/\text{Bi}_4\text{O}_5\text{I}_2$ was propitious to accelerate the transition efficiency and restrain the recombination of surface charge, favoring the improvement of photodegradation ability. The result of EIS analysis was in accordance with the photocurrent.

The electron spin resonance spin-trap technique was applied to confirm the reactive oxygen species produced during the photocatalytic process [56]. In the ESR spin-trap tests, $\text{O}_2^{\bullet-}$ and $\bullet\text{OH}$ radicals can be trapped by DMPO in the methanol dispersion and aqueous dispersion, respectively. Both the characteristic peaks of $\text{DMPO}-\text{O}_2^{\bullet-}$ (Fig. 11a) and $\text{DMPO}-\bullet\text{OH}$ (Fig. 11b) species cannot be detected under visible light irradiation, which indicated that the reactive oxygen species $\text{O}_2^{\bullet-}$ and $\bullet\text{OH}$ could not be generated in this system.

Free radicals trapping experiment was carried out to further determine the main active species during the photocatalytic process. The triethanolamine and *tert*-butyl alcohol was added as trapping agents for holes and $\bullet\text{OH}$, respectively. As shown in Fig. 12, there have almost no change after mixed with *tert*-butyl alcohol,

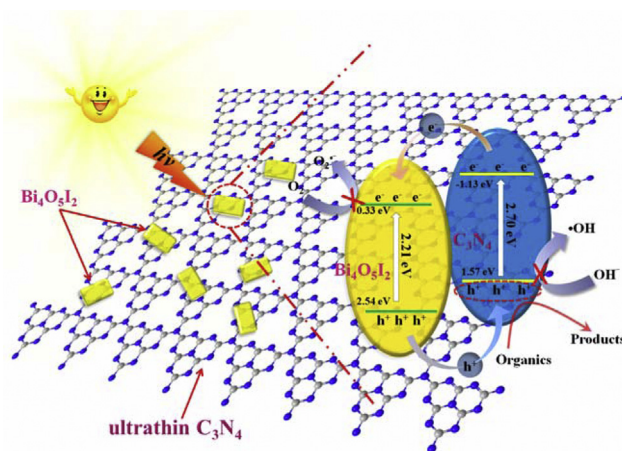


Fig. 13. Schematic of the separation and transfer of photogenerated electron-hole pairs in the ultrathin $\text{C}_3\text{N}_4/\text{Bi}_4\text{O}_5\text{I}_2$ combined with the possible reaction mechanism of photocatalytic procedure.

which revealing the $\bullet\text{OH}$ may not the main active species in this system. It was in consistent with the ESR analysis. After the triethanolamine was added, the inhibitory photocatalytic activity was obviously observed, meaning the hole may play important role in the photocatalytic degradation process. Based on the result of ESR and free radicals trapping experiment, holes played the main roles while the $\text{O}_2^{\bullet-}$ or $\bullet\text{OH}$ radicals were not the main active species during the photocatalytic reaction under visible light irradiation.

On the basis of the DRS analysis, the band gap energy (E_g) of the as-synthesized $\text{Bi}_4\text{O}_5\text{I}_2$ sample was determined using a plot of $(\alpha h\nu)^{1/2}$ vs. photon energy ($h\nu$) to be approximately 2.21 eV. The valence band potentials (E_{VB}) can be estimated by the empirical formula $E_{VB} = X - E^e + 0.5E_g$, where X is the electronegativity of the corresponding semiconductor, E^e is the energy of free electrons on the hydrogen scale, and the conduction band potential (E_{CB}) can be determined by the formula $E_{CB} = E_{VB} - E_g$. The X value for $\text{Bi}_4\text{O}_5\text{I}_2$ was calculated to be 5.93 eV and E^e was 4.5 eV. Thus the E_{VB} and the E_{CB} of $\text{Bi}_4\text{O}_5\text{I}_2$ were estimated to be 2.54 eV and 0.33 eV, respectively. According to the previous reports, the CB and VB potentials of ultrathin C_3N_4 were -1.13 eV and 1.57 eV, respectively. The suited band positions of $\text{Bi}_4\text{O}_5\text{I}_2$ nanosheets and ultrathin C_3N_4 could favor the separation of charge carriers so as to enhance the photocatalytic performance. The holes transferred from the VB of $\text{Bi}_4\text{O}_5\text{I}_2$ to ultrathin C_3N_4 , at the same time, the electrons removed from the CB of ultrathin C_3N_4 to $\text{Bi}_4\text{O}_5\text{I}_2$ in the ultrathin $\text{C}_3\text{N}_4/\text{Bi}_4\text{O}_5\text{I}_2$ heterojunction system, which further suppressed the recombination of the photo-generated electrons and holes effectively. The holes accumulated on the valence band of C_3N_4 (1.57 eV vs NHE) was more negative than the $E^\circ(\bullet\text{OH}/\text{OH}^-)$ (2.38 eV vs NHE) [32], which meant no OH^- was oxidized to produce $\bullet\text{OH}$. At the same time, the electrons accumulated on the conduction band of $\text{Bi}_4\text{O}_5\text{I}_2$ (0.33 eV vs NHE) was insufficient to reduce O_2 to generate $\text{O}_2^{\bullet-}$ since the $E^\circ(\text{O}_2/\text{O}_2^{\bullet-})$ was -0.046 eV vs NHE [57]. Consequently, $\text{O}_2^{\bullet-}$ and OH^- were not the main active species in this composite, while the h^+ played a vital role during the photodegradation process, and the results were in consistent with the ESR spin-trap tests and free radicals trapping experiments.

Based on the above experimental analysis, a possible reaction mechanism of photocatalytic procedure was proposed (as shown in Fig. 13). Firstly, based on the DRS analysis, there were not much difference among the absorption ranges of visible light for the samples, which could be determined the light harvesting did not play key role in enhancing the photocatalytic activity. Secondly, the BET analysis results indicated that there was a very little difference in BET specific surface areas of as-prepared samples, so the specific

surface areas was not the fatal factor in improving the photodegradation ability in this system. Thirdly, the matched energy band structure is undoubtedly beneficial for the effective separation of electron-hole pairs. In this system, both the C_3N_4 and $Bi_4O_5I_2$ can be excited by visible light and generate electron-hole pairs. The electrons would transfer from the CB of C_3N_4 to the CB of $Bi_4O_5I_2$. At the same time, the hole could accumulate on the VB of C_3N_4 and effective separation of electron-hole pairs was obtained. In this ultrathin $C_3N_4/Bi_4O_5I_2$ system, the ultrasmall C_3N_4 nanosheets were uniformly dispersed on the surface of ultrathin C_3N_4 and constructed the tight junction between the two, which favors the transfer of photo-generated charge carriers across the interface and thus accelerate the process of photocatalytic reaction.

4. Conclusion

In summary, a novel visible-light-driven ultrathin $C_3N_4/Bi_4O_5I_2$ layered nanojunctions photocatalyst was prepared in the presence of reactable ionic liquid [Hmim]I via a facile solvothermal method. TEM analysis demonstrated that the ultrasmall $Bi_4O_5I_2$ nanosheets were dispersed on the surface of ultrathin C_3N_4 evenly and the closely heterostructures were formed. After the introduction of ultrathin C_3N_4 , the photocatalytic activities of composites on RhB and BPA degradation under visible light irradiation increased significantly. The enhanced photocurrent response of ultrathin $C_3N_4/Bi_4O_5I_2$ composite could be ascribed to the formation of heterostructures and the high transfer of electrons and holes under visible light irradiation. The holes were the main active radicals during the photodegradation process. This work is meaningful in design and fabricating the ultrathin C_3N_4 -based compounds by hybridizing with other semiconductor materials.

Acknowledgements

This work was financially supported by the National Nature Science Foundation of China (No. 21476098, 21471069 and 21576123), and the science and technology support program of Zhenjiang (SH2014018).

Appendix A. Supplementary data

Supplementary data associated with this article can be found, in the online version, at <http://dx.doi.org/10.1016/j.apcatb.2016.02.058>.

References

- [1] S.W. Cao, J.X. Low, J.G. Yu, M. Jaroniec, *Adv. Mater.* 27 (2015) 2150.
- [2] H. Takashi, K. Jun, D. Kazunari, *Chem. Soc. Rev.* 43 (2014) 7520.
- [3] H.J. Dong, G. Chen, J.X. Sun, C.M. Li, Y.G. Yu, D.H. Chen, *Appl. Catal. B* 134–135 (2013) 46–54.
- [4] J. Di, J.X. Xia, Y.P. Ge, H.P. Li, H.Y. Ji, H. Xu, Q. Zhang, H.M. Li, M.N. Li, *Appl. Catal. B* 168 (2015) 51.
- [5] J. Di, J.X. Xia, M.X. Ji, H.P. Li, H. Xu, H.M. Li, R. Chen, *Nanoscale* 7 (2015) 11433.
- [6] C.M. Li, G. Chen, J.X. Sun, H.J. Dong, Y. Wang, C.D. Lv, *Appl. Catal. B* 160–161 (2014) 383–389.
- [7] J. Li, Y. Yu, L.Z. Zhang, *Nanoscale* 6 (2014) 8473.
- [8] H.F. Cheng, B.B. Huang, Y. Dai, *Nanoscale* 6 (2014) 2009.
- [9] M.L. Guan, C. Xiao, J. Zhang, S.J. Fan, R. An, Q.M. Cheng, J.F. Xie, M. Zhou, B.J. Ye, Y. Xie, *J. Am. Chem. Soc.* 135 (2013) 10411.
- [10] H. Li, J. Shang, Z.H. Ai, L.Z. Zhang, *J. Am. Chem. Soc.* 137 (2015) 6393.
- [11] H. Li, L.Z. Zhang, *Nanoscale* 6 (2014) 7805.
- [12] J. Di, J.X. Xia, S. Yin, H. Xu, L. Xu, Y.G. Xu, M.Q. He, H.M. Li, *J. Mater. Chem. A* 2 (2014) 5340.
- [13] J.X. Xia, S. Yin, H.M. Li, H. Xu, L. Xu, Y.G. Xu, *Dalton Trans.* 40 (2011) 5249.
- [14] J.X. Xia, J. Di, S. Yin, H. Xu, J. Zhang, Y.G. Xu, L. Xu, H.M. Li, M.X. Ji, *RSC Adv.* 4 (2014) 82.
- [15] H.P. Li, J.Y. Liu, X.F. Liang, W.G. Hou, X.T. Tao, *J. Mater. Chem. A* 2 (2014) 8926.
- [16] L. Zhang, W.Z. Wang, S.M. Sun, Y.Y. Sun, E.P. Gao, Z.J. Zhang, *Appl. Catal. B* 148–149 (2014) 164.
- [17] J. Jiang, K. Zhao, X.Y. Xiao, L.Z. Zhang, *J. Am. Chem. Soc.* 134 (2012) 4473.
- [18] J. Di, J.X. Xia, Y.P. Ge, L. Xu, H. Xu, M.Q. He, Q. Zhang, H.M. Li, *J. Mater. Chem. A* 2 (2014) 15864.
- [19] L.Q. Ye, L. Zan, L.H. Tian, T.Y. Peng, J.J. Zhang, *Chem. Commun.* 47 (2011) 6951.
- [20] H.J. Zhang, Y.X. Yang, Z. Zhou, Y.P. Zhao, L. Liu, *J. Phys. Chem. C* 118 (2014) 14662.
- [21] J. Di, J.X. Xia, M.X. Ji, B. Wang, S. Yin, Q. Zhang, Z.G. Chen, H.M. Li, *ACS Appl. Mater. Inter.* 7 (2015) 20111.
- [22] J.X. Xia, J. Di, H.T. Li, H. Xu, H.M. Li, S.J. Guo, *Appl. Catal. B* 181 (2016) 260.
- [23] J. Li, K. Zhao, Y. Yu, L.Z. Zhang, *Adv. Funct. Mater.* 25 (2015) 2189–2201.
- [24] J. Di, J.X. Xia, S. Yin, H. Xu, L. Xu, Y.G. Xu, M.Q. He, H.M. Li, *RSC Adv.* 4 (2014) 14281.
- [25] L.Q. Ye, J.Y. Liu, Z. Jiang, T.Y. Peng, L. Zan, *Appl. Catal. B* 142–143 (2013) 1.
- [26] Y.X. Guo, H.W. Huang, Y. He, N. Tian, T.R. Zhang, P.K. Chu, Q. An, Y.H. Zhang, *Nanoscale* 7 (2015) 11702.
- [27] J. Di, J.X. Xia, S. Yin, H. Xu, M.Q. He, H.M. Li, L. Xu, Y.P. Jiang, *RSC Adv.* 3 (2013) 19624.
- [28] J. Di, J.X. Xia, Y.P. Ge, L. Xu, H. Xu, J. Chen, M.Q. He, H.M. Li, *Dalton Trans.* 43 (2014) 15429.
- [29] X.C. Zhang, T.Y. Guo, X.W. Wang, Y.W. Wang, C.M. Fan, H. Zhang, *Appl. Catal. B* 150–151 (2014) 486.
- [30] L.M. Sun, L. Xiang, X. Zhao, C.J. Jia, J. Yang, Z. Jin, X.F. Cheng, W.L. Fan, *ACS Catal.* 5 (2015) 3540.
- [31] J. Shang, W.C. Hao, X.J. Lv, T.M. Wang, X.L. Wang, Y. Du, S.X. Dou, T.F. Xie, D.J. Wang, J.O. Wang, *ACS Catal.* 4 (2014) 954.
- [32] J. Di, J.X. Xia, M.X. Ji, S. Yin, H.P. Li, H. Xu, Q. Zhang, H.M. Li, *J. Mater. Chem. A* 3 (2015) 15108.
- [33] S.M. Sun, W.Z. Wang, L. Zhang, L. Zhou, W.Z. Yin, M. Shang, *Environ. Sci. Technol.* 43 (2009) 2005.
- [34] X. Xiao, C.L. Xing, G.P. He, X.X. Zuo, J.M. Nan, L.S. Wang, *Appl. Catal. B* 148–149 (2014) 154.
- [35] Q.C. Liu, D.K. Ma, Y.Y. Hu, Y.W. Zeng, S.M. Huang, *ACS Appl. Mater. Inter.* 5 (2013) 11927–11934.
- [36] Y.Y. Li, H.C. Yao, J.S. Wang, N. Wang, Z.J. Li, *Mater. Res. Bull.* 46 (2011) 292–296.
- [37] X. Xiao, C. Liu, R.P. Hu, X.X. Zuo, J.M. Nan, L.S. Li, L.S. Wang, *J. Mater. Chem.* 22 (2012) 22840–22843.
- [38] W.L.W. Lee, C.S. Lu, C.W. Chuang, Y.J. Chen, J.Y. Fu, C.W. Siao, C.C. Chen, *RSC Adv.* 5 (2015) 23450–23463.
- [39] Y. Peng, P.P. Yu, H.Y. Zhou, A.W. Xu, *New J. Chem.* 39 (2015) 8321–8328.
- [40] X.C. Wang, K. Maeda, A. Thomas, K. Takanabe, G. Xin, J.M. Carlsson, K. Domen, M. Antonietti, *Nat. Mater.* 8 (2009) 76.
- [41] Y. Wang, X.C. Wang, M. Antonietti, *Angew. Chem. Int. Ed.* 51 (2012) 68.
- [42] Y. Zheng, L.H. Lin, X.J. Ye, F.S. Guo, X.C. Wang, *Angew. Chem. Int. Ed.* 53 (2014) 11926.
- [43] C.J. Huang, C. Chen, M.W. Zhang, L.H. Lin, X.X. Ye, S. Lin, M. Antonietti, X.C. Wang, *Nat. Commun.* 6 (2015) 7698.
- [44] Y. Wang, J.S. Zhang, X.C. Wang, M. Antonietti, H.R. Li, *Angew. Chem. Int. Ed.* 49 (2010) 3356.
- [45] Z. Zhu, Z.Y. Lu, D.D. Wang, X. Tang, Y.S. Yan, W.D. Shi, Y.S. Wang, N.L. Gao, X. Yao, H.J. Dong, *Appl. Catal. B* 182 (2016) 115–122.
- [46] P. Niu, L.L. Zhang, G. Liu, H.M. Cheng, *Adv. Funct. Mater.* 22 (2012) 4763.
- [47] Y.F. Sun, H. Cheng, S. Gao, Z.H. Sun, Q.H. Liu, Q. Liu, F.C. Lei, T. Yao, J.F. He, S.Q. Wei, Y. Xie, *Angew. Chem. Int. Ed.* 51 (2012) 8727.
- [48] Y.D. Hou, A.B. Laursen, J.S. Zhang, G.G. Zhang, Y.S. Zhu, X.C. Wang, S. Dahl, I. Chorkendorff, *Angew. Chem. Int. Ed.* 52 (2013) 3621.
- [49] Z. Ma, J.H. Yu, S. Dai, *Adv. Mater.* 22 (2010) 261.
- [50] W.J. Shan, Y. Hu, Z.G. Bai, M.M. Zheng, C.H. Wei, *Appl. Catal. B* 188 (2016) 1–12.
- [51] Q.J. Xiang, J.G. Yu, M. Jaroniec, *J. Phys. Chem. C* 115 (2011) 7355.
- [52] J.G. Yu, J.X. Low, W. Xiao, P. Zhou, M. Jaroniec, *J. Am. Chem. Soc.* 136 (2014) 8839.
- [53] C.M. Li, G. Chen, J.X. Sun, Y.J. Feng, J.J. Liu, H.J. Dong, *Appl. Catal. B* 163 (2015) 415–423.
- [54] C. Han, Z. Chen, N. Zhang, J.C. Colmenares, Y.J. Xu, *Adv. Funct. Mater.* 25 (2015) 221.
- [55] L. Zhang, H.B. Wu, Y. Yan, X. Wang, X.W. Lou, *Energy Environ. Sci.* 7 (2014) 3302.
- [56] Y.H. Lv, Y.Y. Zhu, Y.F. Zhu, *J. Phys. Chem. C* 117 (2013) 18520–18528.
- [57] L.Q. Ye, J.N. Chen, L.H. Tian, J.Y. Liu, T.Y. Peng, K.J. Deng, L. Zan, *Appl. Catal. B* 130–131 (2013) 1.